PERGAMON

Chemical Engineering Science 56 (2001) 2531–2541

Chemical Engineering Science

www.elsevier.nl/locate/ces

A numerical study on the coupling of hydrodynamics and orthokinetic agglomeration

E. D. Hollander[a,b,*], J. J. Derksen[a], O. S. L. Bruinsma[b], H. E. A. van den Akker[a], G. M. van Rosmalen[b]

[a]*Kramers Laboratorium voor Fysische Technologie, Prins Bernhardlaan 6, Delft University of Technology, 2628 BW Delft, Netherlands*
[b]*Laboratory for Process Equipment, Leeghwaterstraat 44, Delft University of Technology, 2628 CA Delft, Netherlands*

Abstract

Numerical studies on orthokinetic agglomeration in a turbulent channel flow and in a stirred tank are presented. By using a lattice Boltzmann scheme to simulate the turbulent flow field, and a Monte Carlo algorithm to solve the particle size distribution, the dependence of the agglomeration rate on the shear rate and the turbulent transport of particles is investigated. It is found that local flow information is needed to model agglomeration and that a description in terms of a volume-averaged agglomeration rate constant β_0 is inadequate for both geometries. Furthermore, turbulent transport of particles is found to be an important factor in the overall agglomeration rate.

Keywords: Orthokinetic; Agglomeration; Hydrodynamics; Turbulence

1. Introduction

The observation that agglomeration of particles in the micrometer size range is largely affected by fluid flow, has first been formulated by von Smoluchowski (1917). Implementing this shear-rate-dependent agglomeration rate in models for industrial purposes has, however, been close to impossible up to now. The reason for this is that the flow field in industrial reactors (stirred tanks) is very complex. Fluid flow in these devices is inherently transient, highly turbulent and contains a large spread in shear rates. To simplify the modelling aspect of the agglomeration process, the agglomeration rate is usually coupled to the volume-averaged energy dissipation rate. An obvious drawback of this approach is that details of the process cannot be predicted under this simplification.

In this research, an attempt has been made to investigate the influence of hydrodynamics on agglomeration in more detail. By using a lattice Boltzmann algorithm with a large eddy model to handle turbulence, pseudo-single-phase turbulent fluid flow is simulated; this yields a local and instantaneous description for the shear rates and fluid velocities in the domain. Based on this flow field, a Monte Carlo scheme is used to integrate local population balances in time. The value of the agglomeration kernel used is based on the local flow conditions. Furthermore, the instantaneous flow field is used to redistribute particles across the flow. By letting this scheme proceed in time, the evolution of the particle size distribution (PSD) in the domain can be tracked.

Since both the flow field and the PSDs have to be integrated in time, simulations will be computationally demanding. To limit the computational effort, a relatively simple flow domain was chosen for a first investigation: a turbulent channel flow, at a Re number of 4800. Although its time-averaged behaviour can be regarded as one dimensional, the instantaneous flow field is three dimensional in nature. Due to the wide range of energy dissipation rates encountered in the channel, this geometry still preserves a lot of the interesting transport phenomena that occur in industrial agitated precipitators. An additional advantage of this approach is that channel flows have been studied extensively in literature, which allows for a critical validation of the computed flow field.

* Corresponding author.

0009-2509/01/$ - see front matter
PII: S0009-2509(00)00435-8

In addition to the channel, the flow in a baffled stirred tank, equipped with a standard Rushton turbine has been simulated. The *Re* number was 1×10^4, which is a value typically encountered in laboratory-scale experiments. Instead of making use of the Monte Carlo method, the particle number concentration was integrated by making use of the analytical solution to size-independent agglomeration. This was done to limit the computational times for the stirred tank simulation.

In Section 2, the theoretical elements of this work are treated. Section 3 contains the numerical details of the two flow cases, i.e. the turbulent channel and the stirred tank. The results are presented in Section 4. Finally, Section 5 is used for discussion and concluding remarks.

2. Theoretical background

2.1. Particle collision mechanism in turbulent flows

Fig. 1 shows a schematic representation of the agglomeration mechanism. An essential step in this mechanism is the collision of particles. For particles with a diameter of approximately 10 μm in water (typical conditions for precipitating systems), collisions may either be caused by velocity gradients or fluid acceleration (Kruis & Kusters, 1997). If it is assumed that particles follow the streamlines exactly, a velocity gradient will cause particles to approach each other. The collision rate can be defined as the product of the square of the particle number concentration and a rate constant or kernel:

$$r = -\tfrac{1}{2}\beta_{0,\mathrm{coll}} m_0^2. \tag{1}$$

The collision kernel can be formulated as follows (von Smoluchowski, 1917):

$$\beta_{0,\mathrm{coll}} = \tfrac{8}{6}\dot{\gamma} d^3. \tag{2}$$

Since this work considers (inherently three dimensional) turbulent flows, the concept of a one-dimensional velocity gradient is ill-defined. For simplicity, it is assumed that the fluid deformation rate can be taken as a measure for the velocity gradients found in the fluid.

Collisions due to the inertia mechanism are caused by differences in relaxation time between particles with different size. Particles with a short relaxation time can adjust to fluid acceleration more easily than particles with a long relaxation time.

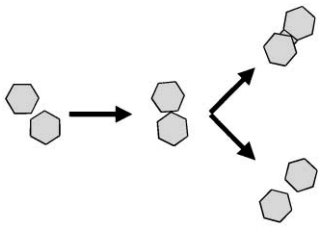

Fig. 1. Agglomeration mechanism.

Saffman and Turner (1956) formulated the total collision kernel for two particles 1 and 2 as

$$\beta = \left(\frac{8\pi}{3}\right)^{1/2}(r_1+r_2)^2\left[\underbrace{3\left(1-\frac{\rho_l}{\rho_p}\right)^2(\tau_1-\tau_2)^2\overline{\left(\frac{\mathrm{D}v_l}{\mathrm{D}t}\right)^2}}_{\text{acceleration}} + \underbrace{\frac{1}{3}(r_1+r_2)^2\frac{\varepsilon}{\nu}}_{\text{shear}}\right]^{1/2}, \tag{3}$$

where the relaxation time τ_i for particles obeying Stokes' law is defined as

$$\tau_i = \frac{(2\rho_p+\rho_l)r_i^2}{9\eta} \tag{4}$$

and $\overline{(\mathrm{D}v_l/\mathrm{D}t)^2}$ is given by (Hinze, 1975, Eqs. (5.59) and (5.63))

$$\overline{\left(\frac{\mathrm{D}v_l}{\mathrm{D}t}\right)^2} = 1.16\varepsilon^{3/2}\nu^{-1/2}. \tag{5}$$

These relations show that the shear mechanism scales with $\varepsilon^{1/2}$, while the accelerative mechanism scales with $\varepsilon^{3/4}$. The relative importance of the mechanisms can be quantified by investigating the ratio of the shear and the acceleration kernel. If one considers calcium oxalate mono-hydrate precipitation in aqueous systems, the material properties are: $\rho_l = 1000\,\mathrm{kg\,m^{-3}}$, $\rho_p = 2200\,\mathrm{kg\,m^{-3}}$, and $\nu = 10^{-6}\,\mathrm{m^2\,s^{-1}}$. A typical value for ε in stirred tank reactors is $0.1\,\mathrm{m^2\,s^{-3}}$. Under these conditions, a collision of a particle with $d_p = 10$ μm and a particle with $d_p = 20$ μm is 10 times more likely to be caused by the shear mechanism, than by inertia effects. This number increases with smaller particle size differences. In this work, it is therefore assumed that collisions are caused by the shear mechanism only.

2.2. Model for shear-rate-dependent agglomeration kernel

Obviously, the collision mechanism is not the only effect present in the agglomeration process. Eq. (3) shows that, at infinitely large energy dissipation rates (i.e. stirring intensely), the number of collisions will be infinitely large. It is known from experiments, however, that the agglomeration rate will fall to zero at very high ε.

Several studies have been presented in literature that try to determine β_0 as a function of average shear rates in stirred tanks (e.g. van Leeuwen, Huizer, Bruinsma, Hounslow, & Van Rosmalen, 1998; Bramley, Hounslow, & Ryall, 1997; Collier & Hounslow, 1999). For this goal,

the shear rate was directly coupled to the impeller speed by the use of relations

$$\dot{\gamma} \propto \sqrt{\frac{\varepsilon}{v}}, \tag{6}$$

$$\bar{\dot{\gamma}} \propto \sqrt{\frac{\bar{\varepsilon}}{v}} = \sqrt{\frac{P/\rho V}{v}} \propto \sqrt{\frac{PoN^3D^2}{v}}. \tag{7}$$

Eq. (6) is based on the idea that crystals formed in precipitating systems are usually smaller than the smallest scales of turbulence. As a consequence, they will experience the shear rate found at these scales. An estimate for the shear rate at the Kolmogorov micro-scales is given by $\sqrt{\varepsilon/v}$.

If it is assumed that energy is dissipated homogeneously throughout the tank, one arrives at Eq. (7). It has been shown, however, that the assumption of homogeneity is not valid in an agitated tank (Derksen & Van den Akker, 1999).

In 1997, Mumtaz presented a numerical study on the shear rate dependence of the agglomeration kernel (Mumtaz, Hounslow, Seaton, & Paterson, 1997). On the basis of a numerical simulation of a simple shear flow, he derived a relation for the agglomeration rate constant as a function of shear rate (see Fig. 2). In the low shear region, Eq. (2) is found, while in the high shear region, the rate constant quickly drops to zero, due to increased viscous forces on the formed agglomerates and the decreased contact time between primary particles.

To the best of our knowledge, only two papers are known that try and validate this curve experimentally (Mumtaz, Seaton, & Hounslow, 1998; Hollander, Derksen, Bruinsma, & Van den Akker, 1998). Both attempts have not yet been able to (re)produce the curve given in Fig. 2. In this work, the numerically found curve will be used, since at this point it is the only available model for $\beta_0(\dot{\gamma})$.

To be able to use the kinetic relation described in Fig. 2 in a three-dimensional turbulent flow, the proportionality constant for Eq. (6) needs to be specified. This appears to be far from trivial, since this factor is likely to be dependent on the (unknown) details of the turbulence at the microscale. To estimate the order of magnitude of the proportionality factor, the values of the collision rate emerging form Eqs. (2) and (3) (without the inertia effect) are compared. For particles with equal diameter the ratio of the rates can be written as

$$\frac{(8/6)\dot{\gamma}d^3}{\sqrt{(8\pi/9)}d^3\sqrt{\varepsilon/v}} \approx 0.8\frac{\dot{\gamma}}{\sqrt{\varepsilon/v}}.$$

Apparently, for the collision rate, $\dot{\gamma}$ behaves quite similar to $\sqrt{\varepsilon/v}$. Although a proportionality factor of 0.8 seems to arise from this analysis, it is our opinion that the applicability of this number is limited (e.g. to derive Eq. (3), isotropic turbulence is assumed. The flows simulated in this work are clearly more complex). Since the proportionality constant is essentially unknown, but likely to be not very different from 1, the constant is set to 1 in this work, i.e. $\dot{\gamma} = \sqrt{\varepsilon/v}$ for the turbulent flows simulated.

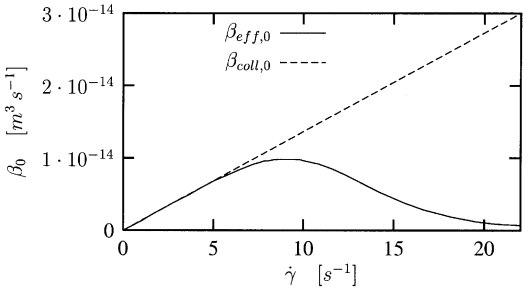

Fig. 2. Shear rate dependence of the agglomeration rate constant β_0 for calcium oxalate mono-hydrate, at a particle size of 10 μm. The dashed line (- - -) represents Eq. (2), the solid line (——) was proposed by Mumtaz.

2.3. The simulation of the single-phase flow field

The lattice Boltzmann method is a relatively new numerical technique for solving the Navier–Stokes equations. Fluid flow is simulated by means of fictitious particles residing on a lattice. The rules describing particle interaction, and the topology of the lattice can be chosen such that, in the incompressible limit the continuity equation and the Navier–Stokes equations (Eqs. (8) and (9)) are solved (Rothman & Zaleski, 1997; Chen & Doolen, 1998; Eggels & Somers, 1995).

$$\nabla\cdot\mathbf{v} = 0, \tag{8}$$

$$\frac{\partial}{\partial t}\mathbf{v} + \mathbf{v}\cdot\nabla\mathbf{v} = -\frac{1}{\rho}\nabla p + \nu\nabla^2\mathbf{v}. \tag{9}$$

A complication encountered frequently in modelling fluid flow in process devices, is the fact that the flow may be turbulent. Although the Navier–Stokes equations (Eq. (9)) still hold for turbulent flows, direct simulation of strong turbulence would require an unrealistically large computational effort. This is due to the fact that the time and space discretisation must at least be able to resolve the smallest turbulent length and time scales λ_k and τ_k, given in

$$\lambda_k = \left(\frac{v^3}{\varepsilon}\right)^{1/4}, \tag{10}$$

$$\tau_k = \left(\frac{v}{\varepsilon}\right)^{1/2}. \tag{11}$$

To overcome this problem, a turbulence model is needed. This model should be able to resolve the flow patterns felt by the crystals. A flow description in terms of the average flow field may not suffice, since the crystals do not experience an average, but rather a local and instantaneous flow. The turbulence models standard to chemical engineering CFD (e.g. the k–ε model) are employed to close the Reynolds-averaged flow equations. These models give an average description of turbulence and therefore do not provide the information needed for studying the agglomeration mechanism in detail. It is for this reason that LES is applied as a turbulence model in this study.

In LES-modelling, the flow field is decomposed into grid scale (GS) and sub-grid scale (SGS) motion. While the GS motion is resolved by the numerical technique used, the SGS motion results in an additional stress tensor in the Navier–Stokes equations. This stress tensor needs to be modelled. In this work, a standard Smagorinsky model is used (Smagorinsky, 1963). The Smagorinsky constant c_s of 0.1 was used for the channel flow simulations, while c_s was 0.12 for the stirred tank simulation. In the latter case, c_s is chosen somewhat larger, to ensure stability of the flow calculation.

2.4. General remarks on suspension modelling

In this study, the suspension is modelled as a 'pseudo-one-phase' fluid. This means that the fluid–particle and particle–particle interactions are disregarded in the flow field computation. This first-order approximation can be justified by the low solids volume fraction ϕ in the modelled suspension. In this work, a particle number concentration of $\approx 10^{13}\,\mathrm{m}^{-3}$ is used, at an average particle size of 10 μm. As a result, ϕ is equal to ≈ 0.005. Using Einstein's law of viscosity (Hiemenz, 1986) then yields

$$\eta_{\mathrm{obs}} = \eta_{fl}(1 + 2.5\phi) = 1.0125\eta_{fl}, \tag{12}$$

where η_{obs} is the observed viscosity. This shows that the one-phase approximation is allowed. Moreover, as was discussed in Section 2.3, the smallest scales of turbulence are modelled by a (rather crude) eddy viscosity model. Since this SGS model is already introducing model errors, detailed models for the influence of the particles on the fluid would imply an amount of detail that is not justified.

Particle transport is incorporated under the assumption that inertia effects are small, and gravity effects are negligible. Particles will therefore follow the streamlines of the fluid and have zero slip velocity. This assumption can be justified by checking the particle relaxation time (Eq. (4)), which is $\mathcal{O}(15\ \mu\mathrm{s})$ for COM-particles of 10 μm in water. Since turbulent timescales are seldomly smaller than 1 ms, it can be seen that particles can easily keep up with the changes in the flow. A major advantage of this simplification is that it is not needed to integrate the particles equations of motion, and that a rather simple particle tracking technique will suffice.

The crystals are redistributed across the flow domain, by making use of the resolved velocities of the flow field calculation. Redistribution due to unresolved (SGS) motion is ignored in this study. This simplification is justified as the kinetic energy of the SGS motion is usually much smaller than that of the resolved flow. In Hollander, Bruinsma, Derksen, van Rosmalen, and van den Akker (2000), a more detailed study is presented on the influence of a SGS model on particle displacement. Small differences were found between simulations of particle movement with and without taking SGS motion into account.

2.5. Monte Carlo integration for PSDs

To determine the influence of hydrodynamics on the agglomeration rate, a PSD-grid is superimposed on the lattice-Boltzmann grid. On this PSD-grid, the local size distributions are subjected to the local hydrodynamic conditions derived from the fluid flow calculations. The integration of the PSDs is done by a Monte Carlo (MC) technique for the channel flow and an analytical technique for the stirred tank reactor.

A lot of research has been done on MC integration of PSDs (van Peborgh Gooch & Hounslow, 1996; Smith & Matsoukas, 1998). Usually, MC algorithms are event-driven. This implies that the PSD is updated after an event (agglomeration, break-up, etc.) has occurred. This formulation gives no direct description for time, the elapsed time has to be calculated from the average frequency of events and the number of events that have occurred. This formulation is of no use in this study, since the flow field calculation imposes the agglomeration time on the MC scheme.

In this work, a time-driven MC algorithm is used (Rajamani, Pate, & Kinneberg, 1986). This algorithm allows for size (in)-dependent agglomeration, size (in)-dependent breakage, growth, nucleation, etc. Here only size-independent agglomeration is incorporated for two reasons: (1) The model for β_0 given in Mumtaz' work predicts a very weak dependence on size only and (2) the MC algorithm can be simplified drastically, decreasing computational effort. The algorithm is given in Algorithm 1.

Algorithm 1. The Monte Carlo step. In the time-driven MC-step the fluid time step is discretized, and the PSD is integrated from t_{start} to t_{end}. Several MC simulations are performed to obtain adequate statistics. The average quantities are used as initial conditions for the next MC step.

Determine β_0 from the local flow field
Obtain PSD from previous timestep

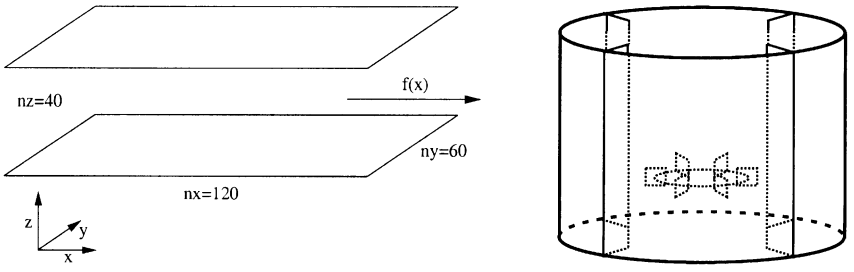

(a) Channel (b) Stirred tank

Fig. 3. Flow domains.

Set $t_{\text{start}} = 0$ and $t_{\text{end}} = \Delta t_{\text{fluid}}$.
for $n = 1,2,\ldots,$ number of MC-runs to obtain statistics **do**
  $t = t_{\text{start}}$
  while $t \leqslant t_{\text{end}}$ **do**
    determine Δt_{MC}, update t.
    Pick random number R, to see if agglomeration event has occurred.
    if agglomeration event **then**
      Handle agglomeration event
    end if
  end while
end
Store new PSD based on the average of the MC-integration.

2.6. Integration of the PSD based on the analytical solution

Although the MC method is flexible for very complex kinetics, it is an overkill for integration of PSDs when only size-independent agglomeration is considered. In this case, an analytical solution strategy for integrating the PSD can be used. If one considers all flow field cells to be a set of interconnected ideally stirred tanks, a set of equations like Eq. (13) fully describes the agglomeration process

$$\frac{\mathrm{d}m_0}{\mathrm{d}t} = -\frac{1}{2}\beta_0(t)m_0^2 - \nabla\cdot(m_0\mathbf{v}). \tag{13}$$

Only one scalar (the number concentration m_0) has to be stored at all the gridnodes and integration can be done with a simple finite differencing scheme in this approach. Obviously, this technique is quicker than the Monte Carlo scheme, and is therefore used for the computationally more intensive stirred tank simulation.

One can now decompose Eq. (13) into a transport step, which redistributes the particles according to the resolved flow field, and a reaction step, in which the local number concentration is updated according to the local initial number concentration and the local agglomeration rate constant. For the transport step, the fluid velocities computed by the lB-scheme are used to determine the fluxes at the cell faces of the MC-grid. Based on these fluxes, particles are transported to and from the six surrounding cells (i.e. top, bottom, left, right, front, back). For the reaction step, the local value for ε is substituted in Eq. (6) for every MC-grid cell. The resulting estimate for the shear rate is then used in the kinetic model by Mumtaz, yielding a local description for β_0.

3. Numerical setup

3.1. Choice of domain size

The flow field calculation can be characterised by the *Re* number only. For the integration of the population balance, however, the flow scales have to be translated to dimensional form. By choosing two scales (a length and a time scale), the flow field and the population balance are coupled.

The flow domain for the turbulent channel flow has a size of $120\times60\times40$ cells (see Fig. 3). At a force of 1.4×10^{-5} l.u.,[1] the centreline velocity is ≈ 0.12 l.u. The chosen dimensionless viscosity is 0.001 l.u., yielding a *Re* number based on the channel height of

$$Re = \frac{vd}{\nu} \approx 4800.$$

The agglomeration kernel computed by Mumtaz predicts an optimum β_0 at a shear rate of $10\ \mathrm{s}^{-1}$. Therefore, the dimensional time scale has been fixed to approximately 0.1 s (in this study, Δt is chosen to be 0.06 s). In the lattice Boltzmann scheme, viscosity scales as h^2/t and

[1] In the lattice Boltzmann scheme, variables are expressed in lattice units (l.u.). The unit of length is "gridspacing", the unit of time is "time step" and the unit of mass is "lB particle mass".

with the viscosity ratio $\nu_{real}/\nu_{lB} = 10^{-6}/10^{-3} = 10^{-3}\ m^2\ s^{-1}$, the appropriate length scale of one cell is found to be 7.75×10^{-3} m. The channel height is thus 31 cm.

The domain for the stirred tank flow has a size of $90 \times 100 \times 100$ cells ($h \times w \times d$). At an impeller diameter of 30 l.u., a rotational speed of 1.06×10^{-3} l.u. and a viscosity of 9.55×10^{-5} l.u., the Re number of this flow:

$$Re = \frac{ND^2}{\nu} \approx 10^4. \tag{14}$$

The real dimensions of this geometry are $D = 0.1$ m, $N = 1\ rev\ s^{-1}$, and $\nu = 10^{-6}\ m^2\ s^{-1}$. The Po number for a Rushton turbine at a Re number of 10^4 is approximately 5, resulting in an average shear rate of $\approx 48.5\ s^{-1}$.

3.2. Choice of number concentration in MC-algorithm

To obtain adequate statistics for the MC integration, an initial number of 1000 particles was found to be sufficient in this study. Since typical number concentrations found in agglomerating suspensions are 10^{12}–$10^{13}\ m^{-3}$, these particles can be considered as a representative sample of the total number of particles in the system. The agglomeration rate constant is rescaled to a system with a number concentration of $10^{13}\ m^{-3}$

$$\beta_{0s} = \beta_{0r} \Big/ \frac{N_{MC}}{m_{0r}}. \tag{15}$$

N_{MC} is the number of MC particles per MC-cell. This procedure is similar to changing the units of β_0 from $m^3\ s^{-1}$ to e.g., $mm^3\ s^{-1}$. In practice, this means that the MC integration is performed in a sub-volume of $(4.64 \times 10^{-4})^3\ m^3$ at a particle number concentration of $10^{13}\ m^{-3}$.

3.3. Monte Carlo grid

To determine the flow field dependence of the agglomeration rate, a MC grid is superimposed on the CFD grid, as was mentioned in Section 2.5. The resolution of the flow field computation is kept constant, while the MC grid has a varying resolution. All flow cells covered by a MC-cell are averaged, yielding a flow description at the resolution of the MC grid. These averaged flow conditions are used to determine the agglomeration rate constant and the particle fluxes at the MC-cell edges. By increasing the MC resolution, more details of the flow field are incorporated (see Fig. 4).

Two limiting cases can be defined. When only one MC-cell is used, a volume-averaging procedure similar to Eq. (7) is being applied. At $120 \times 60 \times 40$ MC-cells, on the other hand, equal resolutions for both the CFD grid and the MC grid are used. The various runs performed are given in Table 1.

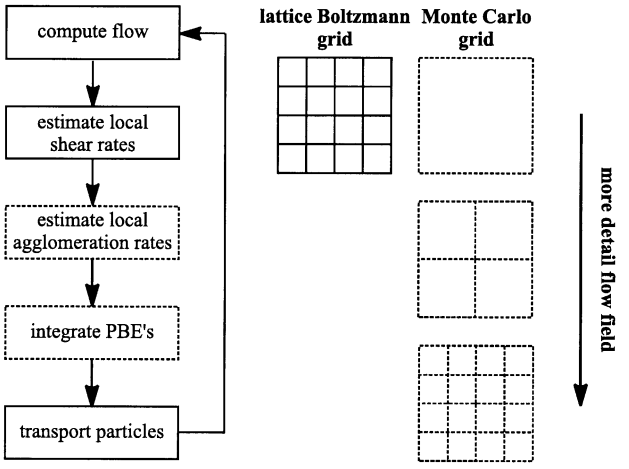

Fig. 4. Schematic representation of the MC grid refinement procedure. Solid lines (——) indicate the CFD grid. By increasing the number of MC cells (- - - - -), the flow field is incorporated in more detail.

Table 1
Resolution of the MC grid in the channel flow runs performed

Run	nx	ny	nz
1	1	1	1
2	10	10	10
3	20	20	20
4	40	30	40
5	120	60	40

3.4. Boundary and initial conditions

Boundary conditions for the turbulent channel flow field are given by two sets of periodic boundaries (at the $x = 0$ and nx plane, and at the $y = 0$ and ny plane), and a set of no-slip boundaries (at the $z = 0$ and nz plane). To improve the behaviour of the LES-model in the near-wall region, a wall damping function is incorporated (van Driest, 1956).

The initial condition for the flow field used in the simulations is a fully developed turbulent channel flow. Initial conditions for the MC cells are a set of particle volumes that are sampled from an exponential distribution. The particles are uniformly distributed across the MC grid.

The top boundary condition of the stirred tank is given by a so-called free-slip condition. The bottom boundary is given by a no-slip wall. The implementation of the curved cylinder wall and the rotating impeller is based on a forcing algorithm (Derksen & Van den Akker, 1999).

This algorithm requires some additional gridnodes between the curved tank wall and the actual boundary of the computational domain.

For this case also, the initial condition was a fully developed turbulent flow, and a uniform particle concentration across the tank was used.

The total procedure is now given in Algorithm 2.

Algorithm 2. Lattice Boltzmann–Monte Carlo code

```
Obtain initial flow field, initialise Monte Carlo grid.
for n = 1,2, ..., number of timesteps do
   solve lattice Boltzmann step.
   if mod(n,10). Eq. (0) then
      (i.e. at every 10th timestep)
      solve Monte Carlo step
      redistribute particles.
   end if
end
Report solution.
```

3.5. Computational demands

For these simulations, a cluster of Pentium III/500 MHz computers with 500 Mb of memory per processor and Linux as an operating system was used. The turbulent channel calculations typically required 70 Mb of memory and 36 h to complete. The stirred tank simulation needed about 180 Mb of memory and took about 1 week. The lattice Boltzmann scheme is relatively easy to parallelize, which makes it possible to increase the size of the simulations, without the need for excessively long computational times.

4. Results

4.1. Turbulent channel flow

In Fig. 5(a), an instantaneous vector plot of the channel flow is shown. It can be seen that turbulent eddies transport fluid from and to the high-shear region near the wall. The average axial velocity is shown in Fig. 5(b). The simulated flow field is validated against the direct numerical simulations at $Re = 3300$, of Kim, Moin, and Moser (1987). The results agree well with their data. Fig. 5(b) also shows that the energy dissipation rate can vary more than one order of magnitude in this geometry.

In Fig. 6, the agglomeration rate constant is plotted as a function of the transverse position in the channel at various MC-resolutions. This figure shows that for this geometry a minimum resolution of $40 \times 30 \times 40$ is needed, to capture the real agglomeration rate constants. The β_0 based on the volume-averaged dissipation rate is found to be 20% larger than the average β_0 based on the local dissipation rates, obtained from the flow field simulation.

The influence of turbulent transport of particles can now be found by comparing the real number concentration in an MC cell and the analytical solution to an agglomeration process (Eq. (13)). By disregarding convective transport and assuming β_0 to be independent of time, Eq. (13) can be integrated to

$$m_0(t) \approx \frac{1}{\frac{1}{2}\beta_0 t + 1/m_{00}}. \tag{16}$$

Neglecting turbulent transport can be valid in two cases, being at zero concentration gradients and at zero fluid velocity. The first case implies that mixing is so fierce, that any particle concentration gradient is immediately levelled. In the second case, no fluid flow is present and the flow system can be considered to be a set of batch reactors with no exchange between the reactors. If one of these conditions holds, then Eq. (16) should provide a correct estimate for the particle number decrease in the domain.

In Fig. 7, the number concentrations at three monitor points from run 4 are compared to the analytical solutions provided by Eq. (16). Due to turbulent transport,

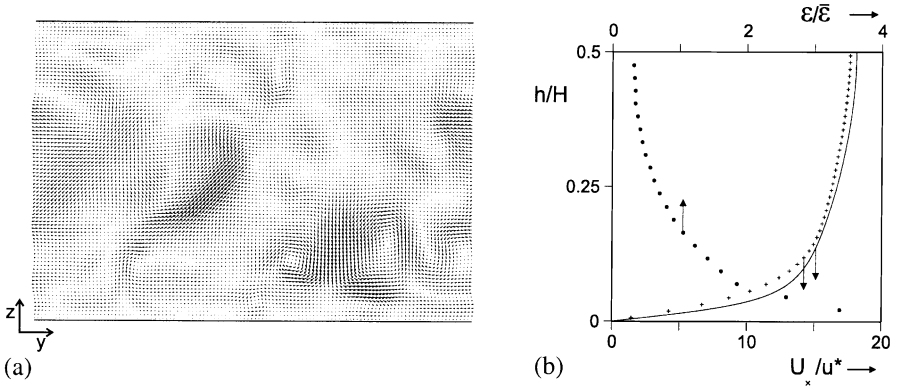

Fig. 5. Validation of flow field. Solid line (——) is curve found by Kim, Moin, and Moser, crosses are values found by lattice Boltzmann technique. Dots (· · · ·) represent the average energy dissipation rate. (a) Instantaneous flow field, $y - z$-plane. The mean flow is directed into the plane of the paper. (b) Average axial velocity and energy dissipation rate, $x - z$-plane.

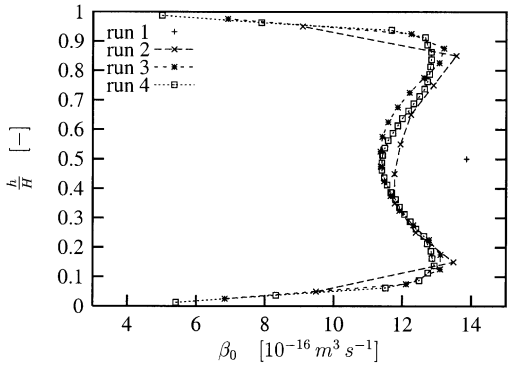

Fig. 6. β_0 at various channel heights and MC resolutions. Run 5 cannot be distinguished from run 4 and is omitted to keep the graph readable.

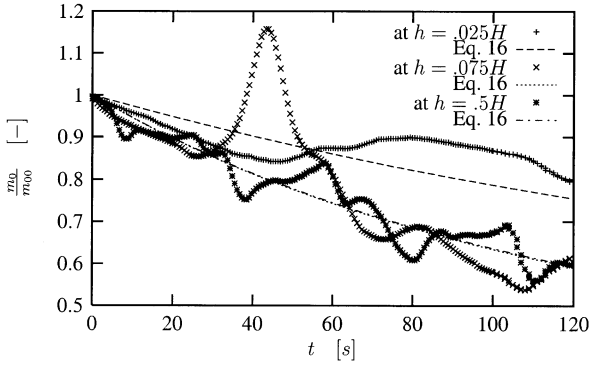

Fig. 7. Number concentration monitored at three points in the flow domain. Results are based on run 4.

the number concentration behaves more irregularly and distinctly deviates from the analytical solution. Apparently, turbulent particle transport is of importance in this process.

As a final test, the average number concentration is compared to the analytical solution based on two estimates for the agglomeration rate constant: β_0 as a function of the volume-averaged dissipation rate and a volume-averaged β_0. Results are given in Fig. 8. It can be seen that the simulated $m_{0,\mathrm{final}}$ differs from both analytical solutions. The difference between the analytical solution, based on local shear rates, and the real simulation is small for this geometry. It is expected that for stirred tanks, this difference will be more pronounced, since the spread in ε will be much higher.

The main conclusion of these results is that turbulent transport of particles plays an important role in the agglomeration process. While it is usually assumed that turbulence levels concentration gradients, it seems that turbulence induces gradients in particle concentration in the agglomeration process. It therefore seems to be insufficient to use a detailed description for β_0 only. Even for this simple geometry, a relatively high resolution for the MC grid is needed. For more complex geometries, the

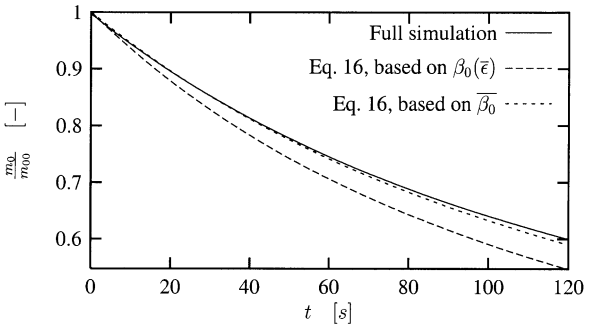

Fig. 8. Number concentration as a function of time. m_0/m_{00} at $t = 120$ s is 0.601, 0.590 and 0.546 for the full simulation, volume-averaged β_0 and β_0 based on the volume-averaged ε, respectively.

lattice Boltzmann grid and the grid for integrating the PSDs should be of comparable resolution.

4.2. Stirred tank

Although the turbulent channel geometry provides a good testcase to study the influence of hydrodynamics on agglomeration, its practical application is limited. Therefore, a simulation of a standard baffled stirred tank with a Rushton turbine was performed as well. Numerical experiments, similar to the turbulent channel were carried out and results are presented here.

In Fig. 9(a), a representation of the flow field in a stirred tank reactor is given. In the impeller region evidence of the so-called "trailing vortices", first described by van't Riet and Smith (1975), can be seen. In Derksen and Van den Akker (1999), the vortices were also found numerically. These coherent structures, that migrate through the tank, can have a large effect on the mixing behaviour of the stirred tank. The fact that a LES-simulation can capture these detailed flow phenomena shows the advantage of using time-dependent techniques for simulating these types of flows.

Fig. 9(b) shows the distribution of ε in a slice through the tank. The left-hand side of this figure shows that, on the average, the energy dissipation rate in the impeller region is several orders of magnitude higher than in the bulk region. On the right-hand side of this figure, it can be seen that ε is distributed irregularly over the domain. This is again caused by the turbulent structures migrating through the tank. Since β_0 is a highly nonlinear function of $\sqrt{\varepsilon}$ (Eq. (6)), the spread in β_0 will be very large.

The presence of flow structures in the turbulent flow shows that the turbulent energy dissipation rate, and therefore the shear rate, is highly distributed over the tank. As a consequence, the agglomeration rate constant is also distributed. Fig. 10 gives an impression of the spread in β_0 in a vertical plane between baffles. The

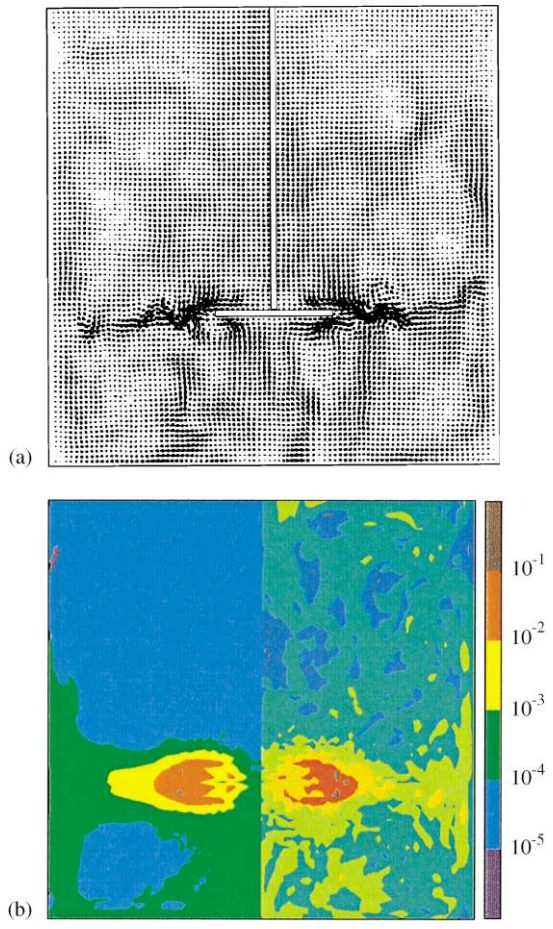

Fig. 9. Features of the simulated turbulent tank flow. (a) Snapshot of the flow field in a vertical plane between the baffles. At the impeller tip region, evidence of the trailing vortices can be found. (b) Turbulent energy dissipation rate in W/kg in a vertical plane between the baffles. The left side is averaged over 50 impeller revolutions, the right side is a snapshot. A log-scale is used for the colour coding.

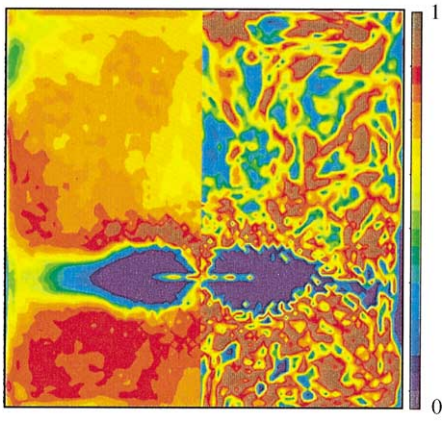

Fig. 10. Normalised agglomeration rate constant β_0 in a vertical plane between the baffles. The left side is averaged over 50 impeller revolutions, the right side is a snapshot.

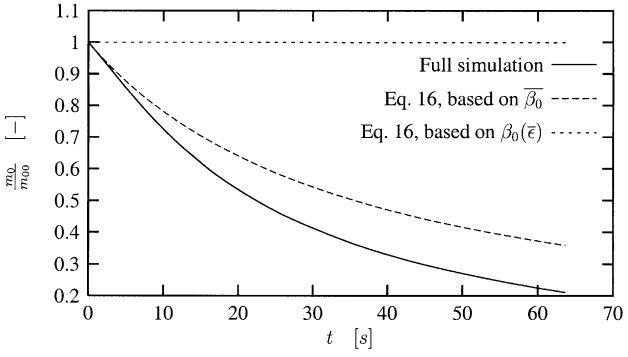

Fig. 11. Number concentration as a function of time for the stirred tank simulation. m_0/m_{00} at $t = 63$ s is 0.21, 0.358 and 0.998 for the full simulation, volume-averaged β_0 and β_0 based on the volume-averaged ε, respectively.

right-hand side of this figure shows an instantaneous realization of β_0. Clearly, structures of high and low agglomeration rate can be distinguished. A somewhat surprising effect can be seen on the left-hand side of Fig. 10. It seems that, on the average, the reactor part below the impeller has a higher β_0 than the region above the impeller. This effect was found in several other cases (Hollander et al., 2000). Apparently, the agglomeration conditions are better in the lower part of the reactor. The total reactor performance, however, is only partly governed by this agglomeration constant. To be able to "use" this high β_0, the particle concentration should remain high in this region. The only mechanism that can accomplish this, is macro-mixing. Macro-mixing and the average β_0 scale-up differently, which may be another reason for the poorly understood scale-up behaviour of the agglomeration process.

In Fig. 11, the relative number concentration of the entire reactor as a function of time shows that the agglomeration rate constant β_0 based on the volume-averaged energy dissipation rate yields unrealistic predictions for the reactor performance. Although the reactor model based on the volume-averaged β_0 seems to perform better, there still is a significant difference between this model and the full simulation. This is yet another indication that it is not possible to determine the agglomeration rate constant from a stirred-tank experiment, as particle transport is a major issue in such an experiment.

5. Conclusions

A simulation tool has been developed that simulates the flow field and the particle size distribution simultaneously. It is found that, for an adequate representation of the agglomeration process, both turbulent transport of particles and the spatial and temporal distribution in energy dissipation rate have to be taken into account. This complex coupling of hydrodynamics and agglomeration makes correct simulation of agglomeration in

a stirred tank computationally intensive and expensive, though it is believed that the technique presented can be used to tackle this problem. Although, for the time being, no experimental evidence is available for validating our results, the computational method looks very promising.

The item of greatest uncertainty in our methodology is the question how the agglomeration constant β_0 depends on the shear rate $\dot{\gamma}$. We used an expression for the collision kernel due to Mumtaz that, however, was never validated experimentally. Measuring this dependence in a stirred vessel is virtually impossible, due to the complex interaction of hydrodynamics and agglomeration. Hence, we claim that the shear rate dependence of the agglomeration should be assessed in dedicated experiments carried out in a simple and well-known flow field such as a Couette flow (Hollander et al., 1998).

Notation

d	characteristic length, m
D	impeller diameter, m
h	z-coordinate, m
H	channel height, m
k	turbulent kinetic energy, $m^2\,s^{-2}$
m_0	zeroth moment, m^{-3}
m_{00}	zeroth moment at $t=0$, m^{-3}
m_{0f}	zeroth moment at $t=t_{final}$, m^{-3}
m_{0r}	real number concentration, m^{-3}
n	simulation counter, dimensionless
N	impeller speed, rev s^{-1}
N_{MC}	number of MC particles, dimensionless
p	pressure, Pa
P	power input, J s^{-1}
Po	power number, dimensionless
r	particle radius, m
R	random number, dimensionless
Re	Reynolds number, dimensionless
t	time, s
u^*	wall-slip velocity, m s^{-1}
U_x	velocity in the x-direction, m s^{-1}
v	velocity, m s^{-1}
$\mathbf{v}$	velocity vector, m s^{-1}
V	volume, m^3

Greek letters

β_0	agglomeration kernel, $m^3\,s^{-1}$
β_{0s}	scaled kernel, $m^3\,s^{-1}$
β_{0r}	real kernel, $m^3\,s^{-1}$
$\dot{\gamma}$	shear rate, s^{-1}
$\bar{\varepsilon}$	average energy dissipation rate, $m^2\,s^{-3}$
ε	energy dissipation rate, $m^2\,s^{-3}$
η_{fl}	dynamic viscosity, Pa s
λ_k	Kolmogorov length scale, m
ν	kinematic viscosity, $m^2\,s^{-1}$
ν_{real}	real kinematic viscosity, $m^2\,s^{-1}$
ν_{lB}	kinematic viscosity of lB scheme, dimensionless
ρ	density, kg m^{-3}
ρ_l	liquid density, kg m^{-3}
ρ_p	particle density, kg m^{-3}
τ	residence time, s
τ_i	relaxation time for particle i, s
τ_k	Kolmogorov time scale, s
ϕ	volume fraction, dimensionless

Acronyms

CFD	computational fluid dynamics
GS	grid scale
LES	large eddy simulation
lB	lattice Boltzmann
l.u.	lattice units
MC	Monte Carlo
PSD	particle size distribution
SGS	sub-grid scale

References

Bramley, A. S., Hounslow, M. J., & Ryall, R. L. (1997). Aggregation during precipitation from solution kinetics for calcium oxalate mono hydrate. *Chemical Engineering Science*, *52*, 747–757.

Chen, S., & Doolen, G. D. (1998). Lattice Boltzmann method for fluid flows. *Annual Review of Fluid Mechanics*, *30*, 329–364.

Collier, A. P., & Hounslow, M. J. (1999). Growth and aggregation rate for calcite and calcium oxalate monohydrate. *A.I.Ch.E. Journal*, *45*(11), 2298–2305.

Derksen, J. J., & Van den Akker, H. E. A. (1999). Large eddy simulations on the flow driven by a rushton turbine. *A.I.Ch.E. Journal*, *45*(2), 209–221.

Eggels, J. G. M., & Somers, J. A. (1995). Numerical simulation of free convective flow using the lattice-Boltzmann scheme. *International Journal of Heat and Fluid Flow*, *16*, 357–364.

Hiemenz, P.C. (1986). Principles of colloid and surface chemistry. 2nd ed. New York: Marcel Dekker, Inc.

Hinze, J. O. (1975). *Turbulence* (2nd ed.). New York: McGraw Hill.

Hollander, E. D., Bruinsma, O. S. L., Derksen, J. J., van Rosmalen, G. M., & van den Akker, H. E. A. (2000). A numerical investigation into the influence of mixing on orthokinetic agglomeration. In *10th European conference on mixing*.

Hollander, E. D., Derksen, J. J., Bruinsma, O. S. L., & Van den Akker, H. E. A. (1998). Measuring the effect of hydrodynamics on agglomeration. In *Proceedings of the 1998 annual AIChE meeting*, Miami (pp. 156–161).

Kim, J., Moin, P., & Moser, R. (1987). Turbulence statistics in fully developed channel flow at low reynolds number. *Journal of Fluid Mechanics*, *177*, 133–166.

Kruis, F. E., & Kusters, K. A. (1997). The collision rate of particles in turbulent flow. *Chemical Engineering Communications*, *158*, 201–230.

Mumtaz, H. S., Hounslow, M. J., Seaton, N. A., & Paterson, W. R. (1997). Orthokinetic aggregation during precipitation: A computational model for calcium oxalate monohydrate. *Transactions of the Institution of Chemical Engineers*, *75*, 152–159.

Mumtaz, H. S., Seaton, N. A., & Hounslow, M. J. (1998). Towards a priori prediction of aggregation rates during crystallization. In *Proceedings of the 1998 annual AIChE meeting*, Miami.

Rajamani, K., Pate, W. T., & Kinneberg, D. J. (1986). Time-driven and event-driven Monte Carlo simulations of liquid–liquid dispersions:

A comparison. *Industrial and Engineering Chemistry Fundamentals*, *25*, 746–752.

Rothman, D. H., & Zaleski, S. (1997). *Lattice-gas cellular automata* (1st ed.). Cambridge: Cambridge University Press.

Saffman, P. G., & Turner, J. S. (1956). On the collision of drops in turbulent clouds. *Journal of Fluid Mechanics*, *1*, 16.

Smagorinsky, J. (1963). General circulation experiments with the primitive equations: 1. The basic experiment. *Monthly Weather Review*, *91*, 99–164.

Smith, M., & Matsoukas, T. (1998). Constant-number Monte Carlo simulation of population balances. *Chemical Engineering Science*, *53*, 1777–1786.

van Driest, E. R. (1956). On turbulent flow near a wall. *Journal of Aerospace Science*, *23*, 1007–1011.

van Leeuwen, M. L. J., Huizer, O. S. L., Bruinsma, C., Hounslow, M. J., & van Rosmalen, G. M. (1998). The influence of hydrodynamics on agglomeration of aluminum hydroxide: An experimental study. In *International conference on mixing and crystallization*.

van Peborgh Gooch, J. R., & Hounslow, M. J. (1996). Monte Carlo simulation of size-enlargement mechanisms in crystallization. *A.I.Ch.E. Journal*, *42*(7), 1864–1874.

van't Riet, K., & Smith, J. M. (1975). The trailing vortex system produced by rushton turbine agitators. *Chemical Engineering Science*, *30*, 1093.

von Smoluchowski, M. (1917). Versuch einer mathematischen theorie der koagulationskinetik koloider lösungen. *Zeitschrift fuer Physikalische Chemie*, *92*, 156.